Inferring Halo Gas Fractions with Mock X-ray Observations of Cosmological Hydrodynamical Simulations

Shera Jafaritabar¹

¹ Universität Heidelberg, Zentrum für Astronomie, ITA, Albert-Ueberle-Str. 2, 69120 Heidelberg, Germany

² Max Planck Institut f
ür Astronomie, K
önigstuhl 17, 69121 Heidelberg, Germany

ABSTRACT

We investigate the baryonic gas content in galaxy clusters through mock X-ray analysis of the IllustrisTNG simulation, comparing it with observational data from Chiu et al. (2018). Chiu et al. estimated the total mass, intracluster medium (ICM) mass, and stellar mass for 91 Sunyaev-Zel'dovich effect (SZE) selected galaxy clusters from the South Pole Telescope (SPT-SZ) survey, utilizing Chandra X-ray observations, optical data from the Dark Energy Survey, and near-infrared photometry from WISE or Spitzer. In this study, we apply a modified β -model, similar to that used by Chiu et al., to estimate gas fractions in halos from the simulation. Our results reveal a significant overestimation of gas fractions in the mock data compared to both the simulation and observational results, likely due to simplified assumptions of spherical symmetry and hydrostatic equilibrium.

The mock data exhibit consistently higher gas fractions than those directly computed from the simulation, indicating that the method inflates the true gas content in galaxy clusters. Moreover, unlike the observational data, which show a clear trend of increasing gas fraction with halo mass, the mock gas fractions remain relatively flat across different halo masses. This discrepancy highlights limitations in the IllustrisTNG feedback mechanisms, particularly AGN feedback, which appear insufficient to expel gas efficiently beyond the halo's virial radius.

These findings suggest that the true gas mass in galaxy clusters is likely lower than current estimates, including those reported by Chiu et al.. Future improvements should focus on incorporating stronger feedback models and exploring more sophisticated X-ray luminosity equations. Extending the analysis to the TNG-Cluster Simulation will also help clarify the efficiency of feedback processes in the most massive halos and improve the accuracy of gas fraction predictions in galaxy clusters.

1. Introduction

1.1. Density, Temperature, and Metallicity

One of the methods to derive the mass of the intracluster medium (ICM) in a halo is through X-ray data, as demonstrated by Chiu et al. (2018). Studies have shown a strong correlation between X-ray luminosity (L_X) and temperature (T) in galaxy clusters. This relationship is typically described by a power law, where higher temperatures correspond to higher luminosities. For instance, in a sample of 31 nearby galaxy clusters, X-ray luminosity exhibited a steep power-law relation with temperature, indicating that luminosity increases more rapidly than expected from self-similar models. This steepening is primarily attributed to variations in gas content with mass, rather than structural differences among clusters (Pratt et al. 2009; Zhang et al. 2011). We will revisit this relation in more detail when calculating X-ray luminosity.

Density and metallicity also play important roles in influencing X-ray luminosity. Observations indicate that higher metallicity is associated with excess luminosity in the L_X -T correlation, suggesting that the presence of heavier elements enhances cooling processes in the hot gas, thereby increasing X-ray emission (Mushotzky 1998). The gas density within clusters significantly impacts the X-ray emissivity, with denser environments exhibiting stronger correlations with X-ray luminosity. Metallicity, particularly in low-density settings, can further influence X-ray emission. Thus, in this research, it is essential to model these quantities using simulations, such as IllustrisTNG, across halos of varying masses.

In astrophysical halos, gas density is often correlated with temperature. Higher density gas is more compressed, leading to elevated temperatures due to increased pressure. This relationship is particularly evident in galaxy clusters, where the hot ICM spans a range of densities and temperatures. The gas temperature in halos is also influenced by virial equilibrium, which relates the total mass of the halo to its temperature. In self-similar models, the expected relation is $T \propto M^{2/3}$. However, deviations from this relation can occur due to processes like cooling flows and feedback from star formation or active galactic nuclei (AGN) (Pratt et al. 2009).

In Figures 1 and 2, we plot mass-weighted temperature and surface density as 2D histograms for halos with masses ranging from $10^{12}M_{\odot}$ to $10^{14}M_{\odot}$. The first row shows results for all temperatures, while the second row focuses on gas with temperatures above 10^6 K. From the first row, we observe that the highest mass-weighted temperatures occur where surface density is also highest—at the halo centers. Comparing the two rows, we see that in lower-mass halos, the particle count decreases, and the deviation from the all-temperature distribution becomes more pronounced.

Metallicity, defined as the abundance of elements heavier than helium, is influenced by gas density. In denser regions, such as halo centers, metals are retained more effectively due to gravitational potential wells, allowing for more efficient recycling of metal-rich gas via galactic winds (Ma et al. 2016). This effect is evident in Figure 3, where the highest mass-weighted metallicity occurs in halo centers.

Additionally, metallicity has a complex relationship with temperature: higher metallicity can enhance cooling processes, while hotter gas tends to have lower metallicity because energetic environments often eject metals from halos. Conversely, cooler gas retains metals more efficiently, leading to higher

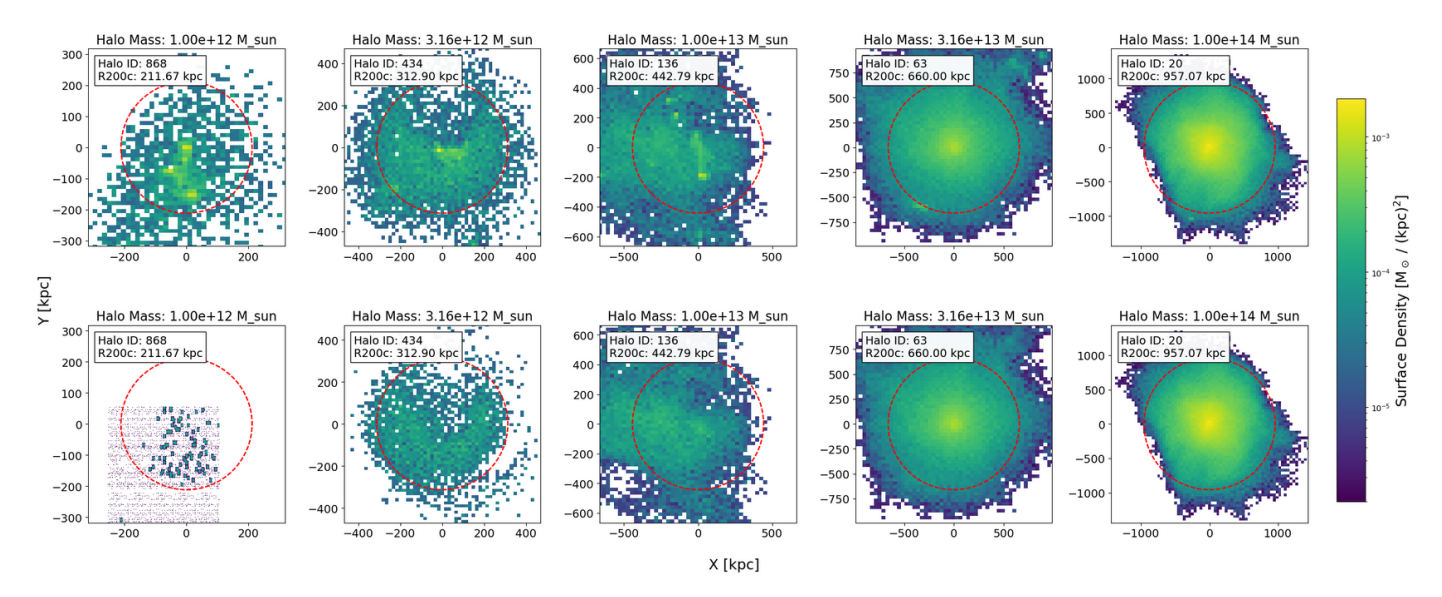


Fig. 1: 2D map of gas surface density for halos with masses between $10^{12} M_{\odot}$ and $10^{14} M_{\odot}$. The first row includes all gas temperatures, while the second row is restricted to gas with temperatures above 10^6 K. Surface density is defined as the gas mass divided by the bin area. The plot limits are normalized to the virial radius, with the halo center at the origin.

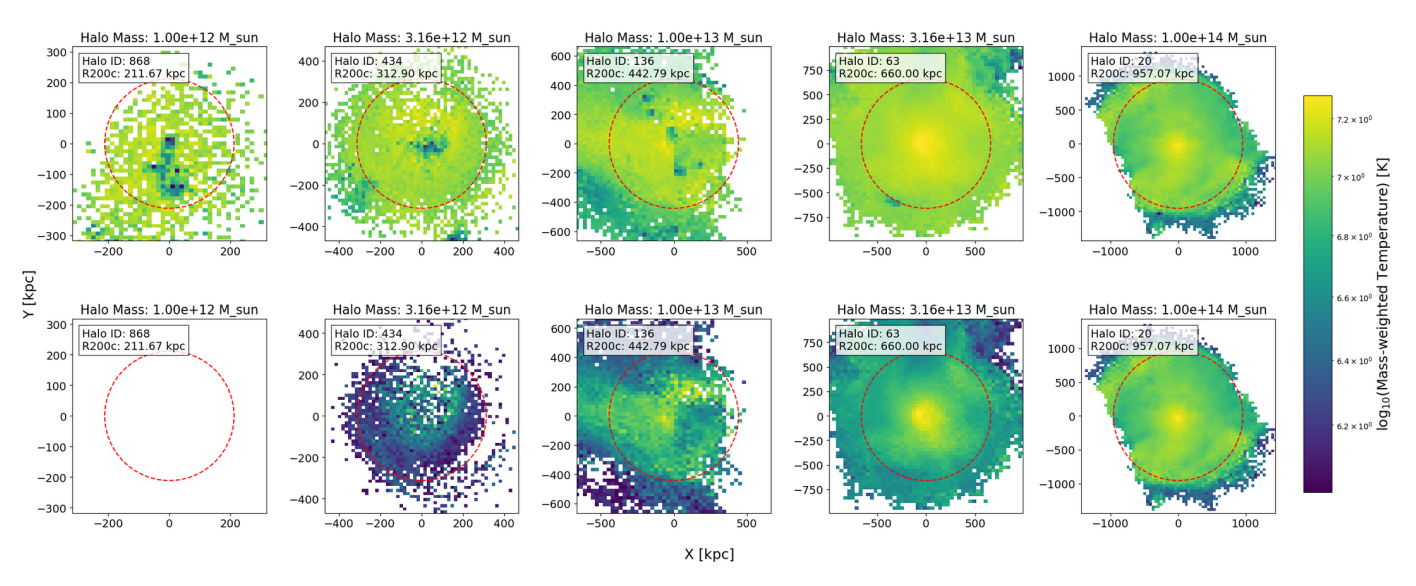


Fig. 2: 2D map of mass-weighted temperature for halos with masses between $10^{12}M_{\odot}$ and $10^{14}M_{\odot}$. The first row includes all gas temperatures, while the second row is restricted to gas with temperatures above 10^6 K. The highest mass-weighted temperatures occur in regions of high gas surface density.

metallicity. This trend is also visible when comparing Figures 2 and 3, where the highest temperatures and metallicities are both concentrated in halo centers.

In conclusion, from Figures 1, 2, and 3, we can draw the following key points:

- 1. Higher gas density correlates with higher temperature due to compression and virial equilibrium.
- 2. Denser regions retain more metals, resulting in higher metallicity.
- 3. Hotter gas generally has lower metallicity due to metal ejection, while cooler gas retains more metals.

1.2. Missing Baryon Problem, Cold and Hot Gas Fraction

The missing baryon problem refers to the discrepancy between the predicted amount of baryonic matter in the universe and what has been observed. According to measurements from the cosmic microwave background (CMB) and Big Bang nucleosynthesis, baryonic matter should account for approximately 4-5% of the universe's total energy density. However, observations indicate that less than half of this baryonic matter is accounted for in the present-day universe, leading to the conclusion that a significant amount of baryons is "missing." These missing baryons are believed to exist primarily in forms that are difficult to detect (Shull et al. 2012), including:

Warm-Hot Intergalactic Medium (WHIM): The WHIM
consists of hot, diffuse gas that fills the space between galaxies and is thought to contain a substantial fraction of the
missing baryons. Direct observation of the WHIM is challenging because it is too diffuse to be easily detected (Nicastro et al. 2018).

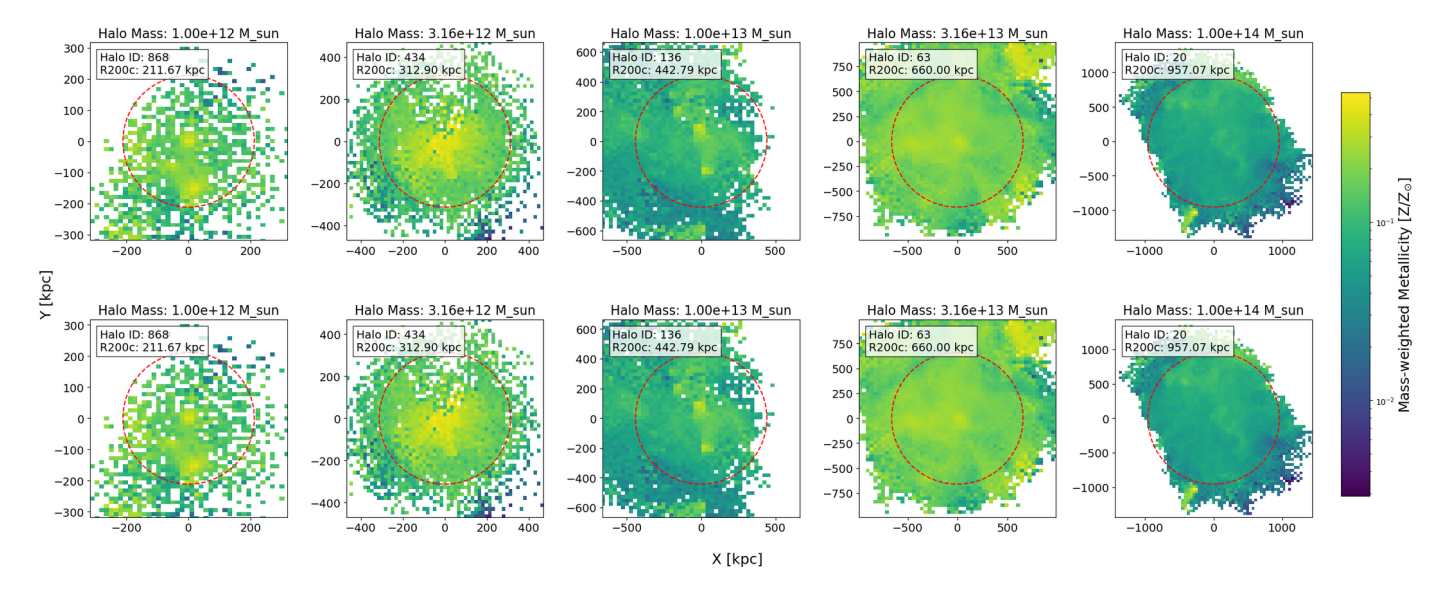


Fig. 3: 2D map of mass-weighted metallicity, normalized by the Sun's metallicity ($Z_{\odot} = 0.0134$). The first row includes all gas temperatures, while the second row is restricted to gas with temperatures above 10^6 K. Higher metallicity is observed in the central regions of the halos, particularly where gas density is also higher.

Circumgalactic Medium (CGM): The CGM is the gas surrounding galaxies, which can harbor a significant amount of baryonic matter. The CGM acts as a reservoir for baryons and plays a crucial role in galaxy formation and evolution.

The fractions of hot and cold gas within halos are also related to the missing baryon problem:

- Hot Gas Fraction: In massive halos, a larger fraction of the baryonic matter exists in the form of hot gas, particularly in the intracluster medium (ICM). The ICM contributes significantly to the baryon budget, accounting for around 4% of the total baryon content, and is primarily composed of ionized hydrogen at high temperatures. Measuring this hot gas fraction is a key objective of this research.
- Cold Gas Fraction: In smaller halos, cold gas dominates the baryonic mass. Cold gas is typically associated with star formation and can be more readily observed. However, feedback processes such as supernovae and active galactic nuclei (AGN) can expel cold gas from halos, contributing to the lower observed baryon fraction, which ties into the missing baryon problem.

IIn Figures 4 and 5, we plot the ratio of different baryonic components to the halo mass, defined as M_{200c} , for the following five components:

- 1. Total halo baryonic mass within R_{200c} : Gas + stars + black holes.
- 2. Total halo gas mass within R_{200c} : Gas only.
- 3. Hot gas within R_{200c} ($T \ge 10^6$ K).
- 4. Cold/cool/warm gas within R_{200c} ($T < 10^6$ K).
- 5. Stellar mass within R_{200c} .

In both figures, the lines represent the median values, and in Figure 4, the shaded region shows the standard deviation. Notably, the y-axis in both figures is normalized by the cosmic baryon fraction (0.157), providing the normalized baryon fraction.

From these results, it becomes evident that in massive halos (with masses exceeding $10^{14} M_{\odot}$), the hot gas fraction approaches unity and closely follows the total baryonic mass. This emphasizes the importance of focusing on hot gas in these systems for the remainder of this research. However, it is also apparent that the stellar mass is approximately one order of magnitude lower in significance, while the cold gas mass is more than two orders of magnitude less important for clusters (halos more massive than $10^{14} M_{\odot}$).

1.3. X-Ray Luminosity

The hot gas fraction in massive halos, such as galaxy clusters, accounts for a significant portion of the total baryonic matter. Simulations suggest that the gas mass fraction approaches the cosmic baryon fraction in high-mass clusters. This implies that a large fraction of the baryons in these systems exists as hot, diffuse gas in the intracluster medium (ICM). The hot gas in the ICM is primarily composed of ionized hydrogen at high temperatures. At these temperatures, the gas emits strongly in X-rays through a process known as thermal bremsstrahlung, in which electrons are accelerated by the electric fields of ions. By studying the X-ray emission from the ICM, we can infer the temperature, density, and metallicity of the hot gas.

For this research, due to time constraints, we use the X-ray luminosity equation from Navarro et al. (1995), given by:

$$L_X = 1.2 \times 10^{-24} (\mu m_p)^{-2} m_g \sum_{i=1}^{N_{gas}} \rho_i T_i^{1/2} \text{ erg s}^{-1}$$
 (1)

where m_g is the mass of a gas particle, ρ_i and T_i are the density and temperature (in keV) at the position of the *i*-th gas particle, m_p is the proton mass, and $\mu = 0.6$ for a fully ionized primordial plasma. Since X-ray emission is primarily associated with hot gas, we will calculate the X-ray luminosity only for gas that meets the hot gas criterion as defined earlier (temperature above 10^6 K).

Using equation 1, we generate a 2D histogram of X-ray luminosity for a sample halo, shown in Figure 6. As expected,

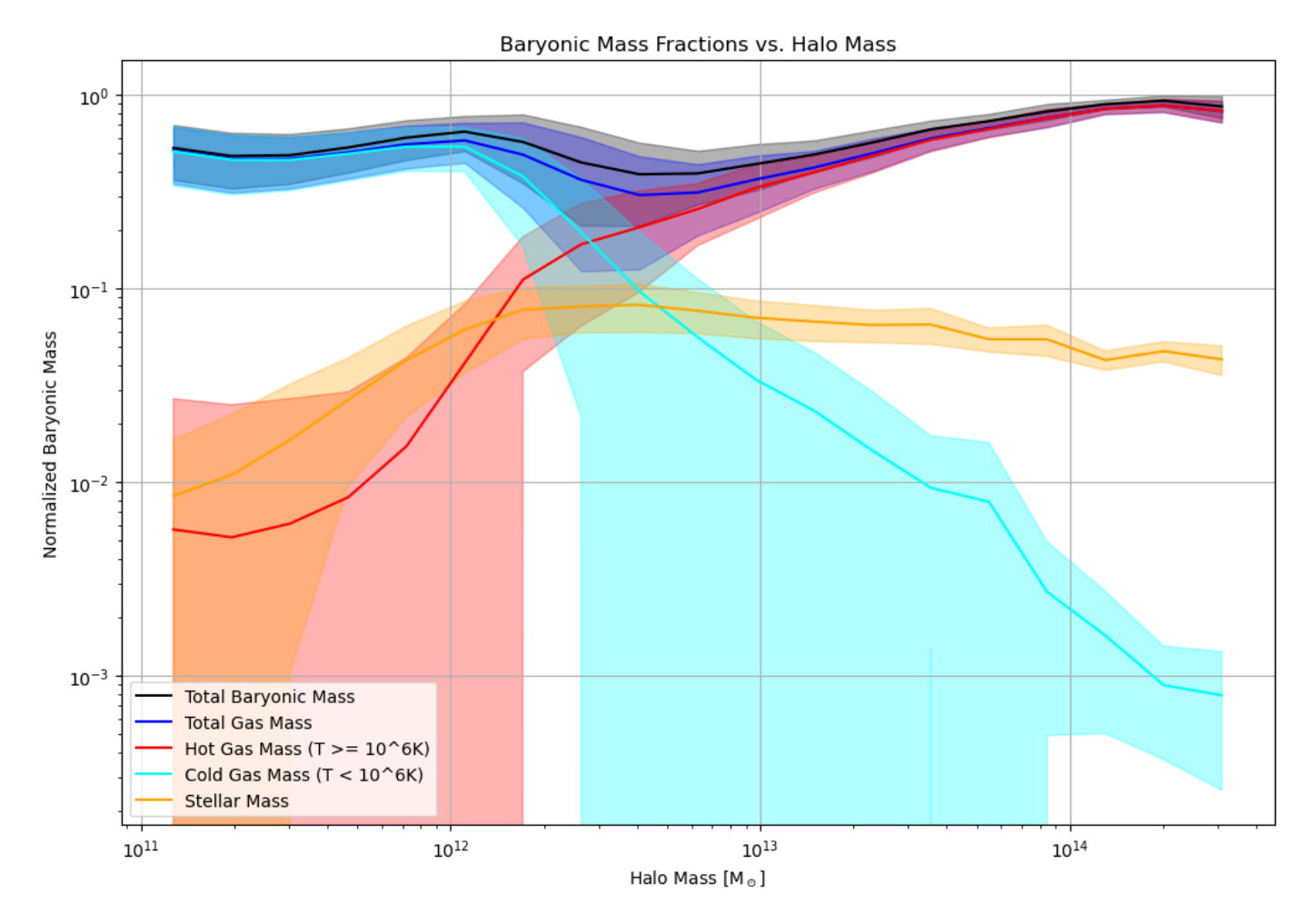


Fig. 4: Normalized baryonic mass by the cosmic baryon fraction (0.157) plotted versus halo mass (M_{200c}) for halos more massive than $10^{11} M_{\odot}$. The five lines represent different baryonic components: total halo baryonic mass (gas + stars + black holes), total halo gas mass, hot gas ($T \ge 10^6$ K), cold gas ($T < 10^6$ K), and stellar mass. The lines show the median values, and the shaded region addresses the standard deviation.

the highest X-ray luminosity is concentrated in the center of the halo, which corresponds to the location of the central galaxy. As we move away from the center, the X-ray luminosity decreases. A similar trend is observed in subhalos, where the central regions exhibit the highest X-ray luminosities.

Similar to Figures 2 and 3, we can compare the mass-weighted temperature and X-ray-luminosity-weighted temperature, using equation 1. As shown in Figure 7, the highest temperatures are located in regions with the highest gas mass or X-ray luminosity, which aligns with the expectation from the relation $L_X \propto T^{1/2}$.

Similarly, Figure 8 compares the mass-weighted and X-ray-luminosity-weighted metallicities. As discussed in previous sections, the highest metallicities occur in the densest regions with the most massive gas, and the same pattern is observed here, where regions with the highest X-ray luminosity also exhibit the highest metallicity.

To validate the use of equation 1 for calculating X-ray luminosity, we compare our results with those of Truong et al. (2024) using the PyXSIM package, which simulates X-ray emission based on gas density, temperature, and metallicity. Figure 9 shows the X-ray luminosity plotted against halo mass for a mock simulation, reproducing the trend seen in Truong et al. (2024). Both plots demonstrate an increase in X-ray luminosity with halo

mass, with similar values for halos of the same mass range. The primary difference is the range of masses and the number of halos in each mass bin, which is limited in our case due to memory constraints (using TNG100-3). This comparison confirms that using equation 1 is a valid approach given the limitations of this research.

2. Methods

The primary goal of this paper is to create a mock X-ray analysis in the IllustrisTNG simulation, following a similar methodology to that used in Chiu et al. (2018). The main steps we will follow are outlined below:

1. **Surface Brightness Profile**: To derive the radial surface brightness profile, we divide the halo into concentric spherical shells of thickness δR . For each shell, we sum over the X-ray luminosity values derived using equation 1. As the goal is to simulate observational data, we project the 3D data onto a 2D surface, which introduces changes to the distribution. For example, a gas particle located far from the center in 3D space may appear closer to the center once projected onto 2D, especially at smaller radii, as shown in Figure 11. The

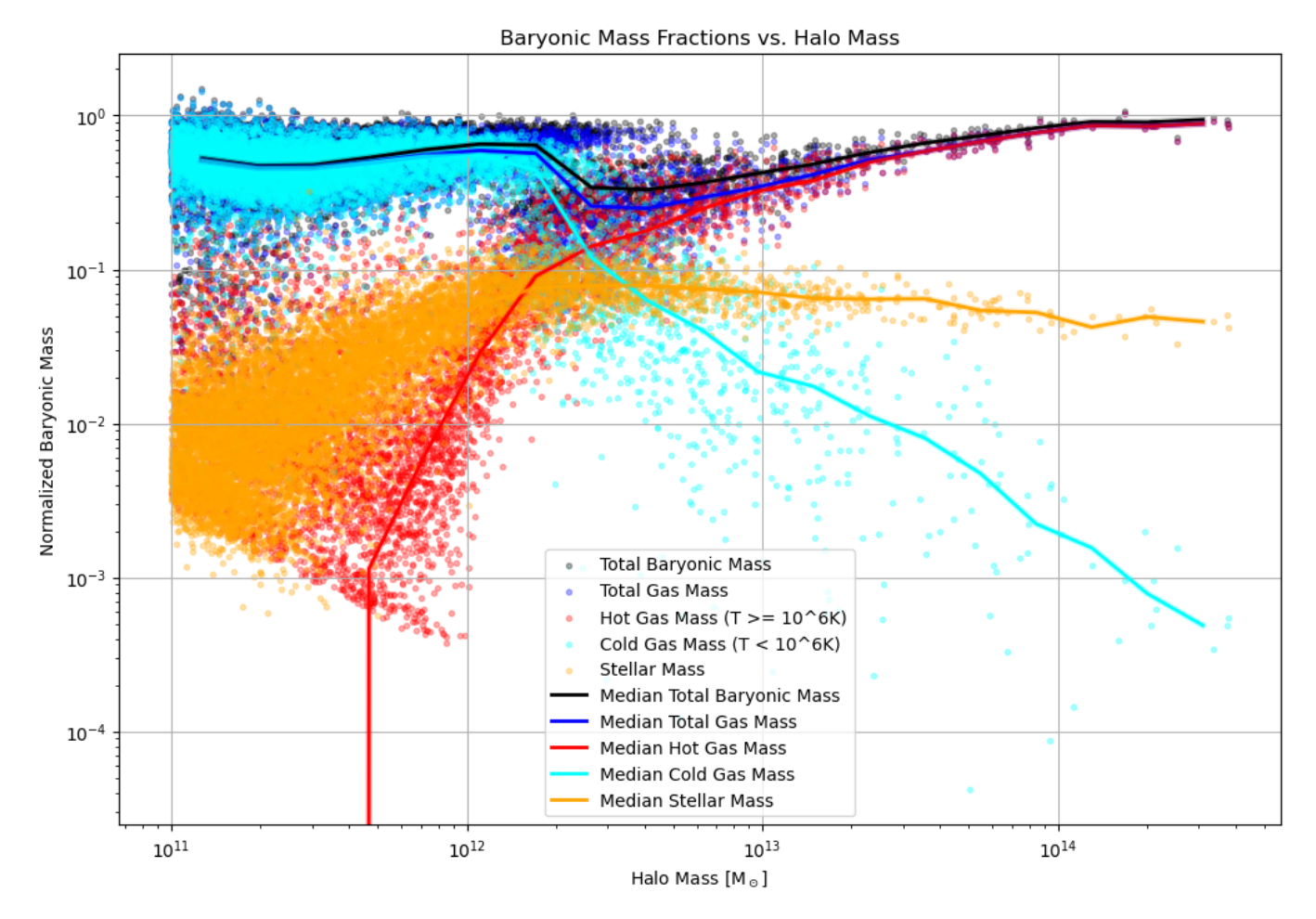


Fig. 5: The ratio of different baryonic components to the halo mass, normalized by the cosmic baryon fraction (0.157), plotted versus halo mass (M_{200c}) for halos more massive than $10^{11} M_{\odot}$. The five lines represent: total halo baryonic mass, total halo gas mass, hot gas ($T \ge 10^6$ K), cold gas ($T < 10^6$ K), and stellar mass. The lines show the median values. The legends have been simplified to improve clarity.

surface brightness in 2D and 3D is computed as follows:

$$S(R) = \frac{L_X}{\pi \left[(R + \delta R)^2 - R^2 \right]},$$
 (2)

We apply this procedure to all halos more massive than $10^{13} M_{\odot}$. The results are displayed in Figure 12. The number of halos used is limited by memory constraints and the use of the TNG100-3 simulation.

2. **Emissivity**: After obtaining the surface brightness, we need to convert it into emissivity. The emissivity can be derived as (Kay & Pratt 2022):

$$EM(r) = 4\pi (1+z)^4 \frac{S(\theta)}{\Lambda(T,z)}, \quad r = d_A(z)\theta, \tag{3}$$

where $S(\theta)$ is the surface brightness, $\Lambda(T, z)$ is the cooling function, and $d_A(z)$ is the angular diameter distance. For the radial profile, the emissivity can be expressed as:

$$EM(r) = (1+z)^4 \frac{S(R)}{\Lambda(T,z)}.$$
 (4)

Setting z = 0 (as we are using snapshot 99 of the simulation), we can plot the emissivity profile, as shown in Figure 13 in black line.

3. **Modified Beta Model**: To fit the emissivity profile, we use the modified β -model, as in Chiu et al. (2018). The modified β -model is expressed as (McDonald et al. 2013):

$$n_e n_p = n_0^2 \frac{\left(\frac{r}{r_c}\right)^{-\alpha}}{\left(1 + \frac{r^2}{r_c^2}\right)^{3\beta - \frac{\alpha}{2}} \left(1 + \frac{r^3}{r_s^3}\right)^{-\frac{\epsilon}{3}}},\tag{5}$$

where n_e and n_p are the electron and proton densities, respectively, n_0 , r_c , r_s , α , β , and ϵ are free parameters to be fitted. Using $n_e = Zn_p$, the gas density can be calculated as:

$$\rho_g^2(r) = \frac{n_0^2 A^2 m_p^2}{Z} \frac{\left(\frac{r}{r_c}\right)^{-\alpha}}{\left(1 + \frac{r^2}{r_c^2}\right)^{3\beta - \frac{\alpha}{2}} \left(1 + \frac{r^3}{r_c^3}\right)^{-\frac{\epsilon}{3}}},\tag{6}$$

where A = 1.397 and Z = 1.199.

To fit the emissivity data, we integrate the β -model along the line of sight, yielding the following integral:

$$\int_{0}^{2r_{vir}} n_e^2 dl = \int_{0}^{2r_{vir}} n_0^2 \frac{\left(\frac{r}{r_c}\right)^{-\alpha}}{\left(1 + \frac{r^2}{r_c^2}\right)^{3\beta - \frac{\alpha}{2}} \left(1 + \frac{r^3}{r_s^3}\right)^{-\frac{\epsilon}{3}}} dl,\tag{7}$$

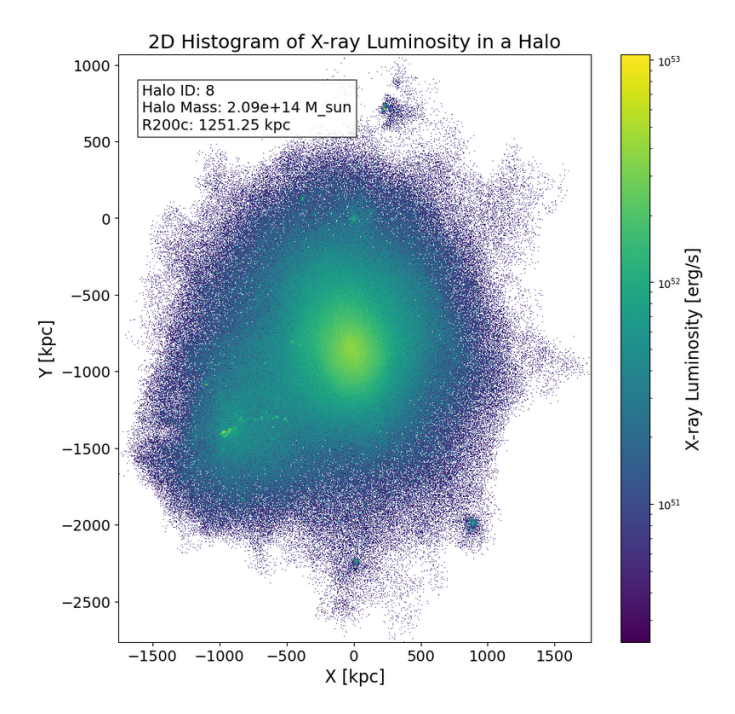


Fig. 6: 2D map of X-ray luminosity for a sample halo, calculated using equation 1. The highest luminosity is observed at the halo center, which is the location of the central galaxy. The luminosity decreases with increasing radial distance from the center.

where $r = \sqrt{R^2 + l^2}$ is the 3D distance, R is the projected radius, and l is the line of sight.

Figure 13 shows the emissivity profile fitted using this modified β -model.

- 4. Once the optimal parameters $(n_0, \alpha, \beta, \epsilon, r_c, \text{ and } r_s)$ are determined from the emissivity fit, we can use equation 6 to calculate the gas density profile. The results are plotted in Figure 14.
- 5. Finally, we integrate the gas density profile over the radial range from 0 to R_{500c} . This gives the mass of the ICM gas $(M_{\rm ICM})$. By dividing this by the total halo mass, we can compute the baryon fraction, which is presented in the results section.

3. Results and Discussion

In this section, we discuss the key findings from our analysis of the mock X-ray data derived from the IllustrisTNG simulation. The primary goal was to study the hot gas fractions within halos and compare these with the corresponding observational data from Chiu et al. (2018). Chiu et al. derived total masses (M_{500}), intracluster medium (ICM) masses (M_{ICM}), and stellar masses (M_*) for a sample of 91 galaxy clusters using data from the South Pole Telescope SPT-SZ survey. This involved a combination of Sunyaev-Zel'dovich effect (SZE) measurements, Chandra X-ray observations, and infrared photometry from DES and WISE/Spitzer. Our analysis reveals significant discrepancies between the gas fractions obtained from simulations, mock data, and observational results.

3.1. Mock Overestimates Gas Fractions Compared to Simulation Data

Our results show a systematic overestimation of gas fractions in the mock data compared to those computed directly from the simulation. Figure 15 presents a comparison between the halo baryon fractions obtained from the simulation data and the mock baryon fractions derived using the methodology described in Section 2.

As illustrated in the top panel of Figure 15, the mock halo baryon fractions are generally higher than the fractions computed directly from the simulation, especially for halos more massive than $10^{14} M_{\odot}$. The bottom panel shows that the ratio of mock to simulation baryon fractions is consistently greater than one, indicating a significant overestimation in the mock approach.

This overestimation likely arises due to the simplified assumptions underlying the mock methodology, particularly the use of the Navarro et al. (1995) equation for X-ray luminosity. This equation, while useful, does not fully capture the complex physics of X-ray emission, such as line emission and cooling effects, which can significantly impact the accuracy of gas fraction estimates. Furthermore, the reliance on hydrostatic equilibrium in mock estimates ignores the potential role of non-thermal pressure support from turbulence and cosmic rays, which are not fully accounted for in the β -model fitting used to infer gas fractions. This limitation is exacerbated in simulations where feedback mechanisms such as AGN-driven winds and supernovae are not as effective in redistributing gas, leading to further discrepancies.

These results suggest that both simulations and observational methodologies may be overestimating the true gas content within galaxy clusters. For future studies, improvements could involve replacing the Navarro et al. (1995) equation with more accurate X-ray models that better account for the full range of physical processes influencing gas distribution.

3.2. Discrepancies Between Mock and Observational Data

A key finding from our analysis is the difference in trends between the mock baryon fractions and those observed in galaxy clusters. In Figure 16, we compare the mock baryon fractions derived from the IllustrisTNG simulation to the observational data from Chiu et al. (2018), which was based on the SPT-SZ survey and Chandra X-ray observations.

As shown in Figure 16, the mock baryon fractions are generally higher than those obtained from the observational data. Additionally, a key difference is the trend with halo mass. In the observational data, we observe a clear positive correlation between the baryon fraction (normalized by $M_{\rm ICM}$) and halo mass, with higher fractions seen in more massive halos. This trend likely reflects the fact that more massive halos are more effective at retaining their gas content, especially hot gas, due to their stronger gravitational potential.

However, in the mock data from the IllustrisTNG simulation, no such trend is observed. The mock baryon fractions remain relatively constant across a wide range of halo masses. This discrepancy suggests that the feedback processes implemented in the simulation may not be sufficiently mass-dependent to replicate the gas retention seen in real galaxy clusters. In particular, AGN feedback in the TNG model may not scale strongly enough with halo mass to reflect the observed increase in gas fractions in more massive systems.

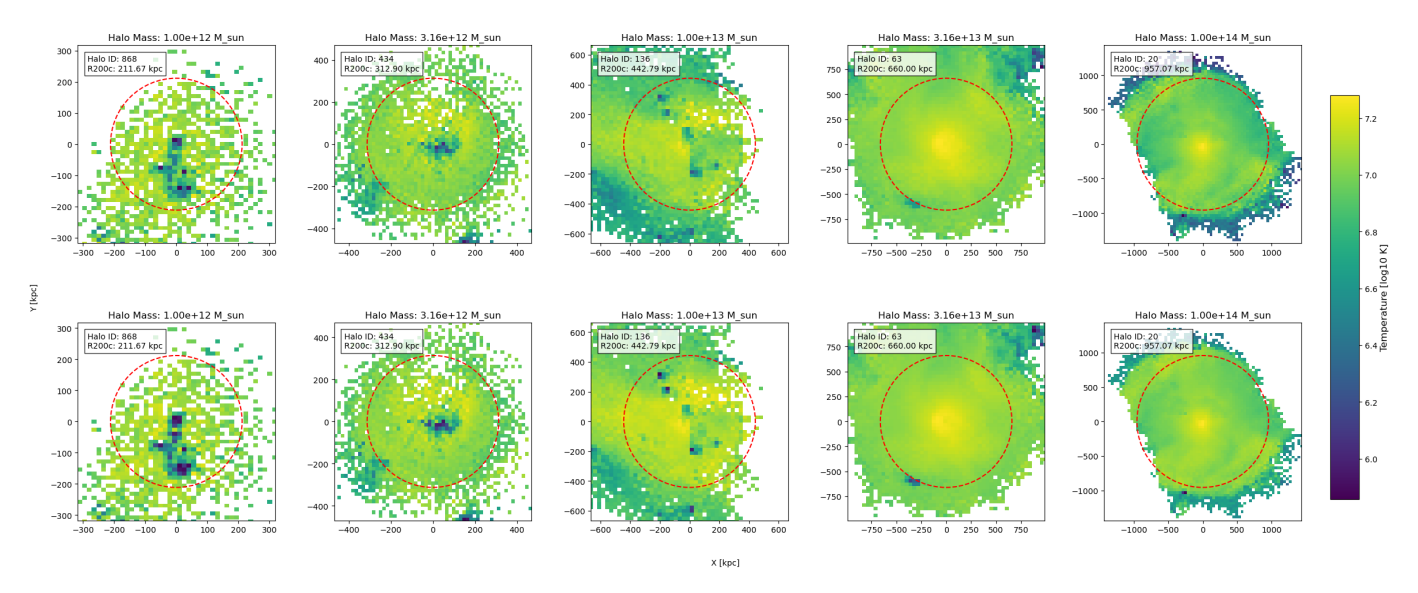


Fig. 7: 2D map of temperature for a sample halo. The first row shows mass-weighted temperature, while the second row shows X-ray-luminosity-weighted temperature, calculated using equation 1. The highest temperatures are concentrated in regions with the highest gas mass or X-ray luminosity.

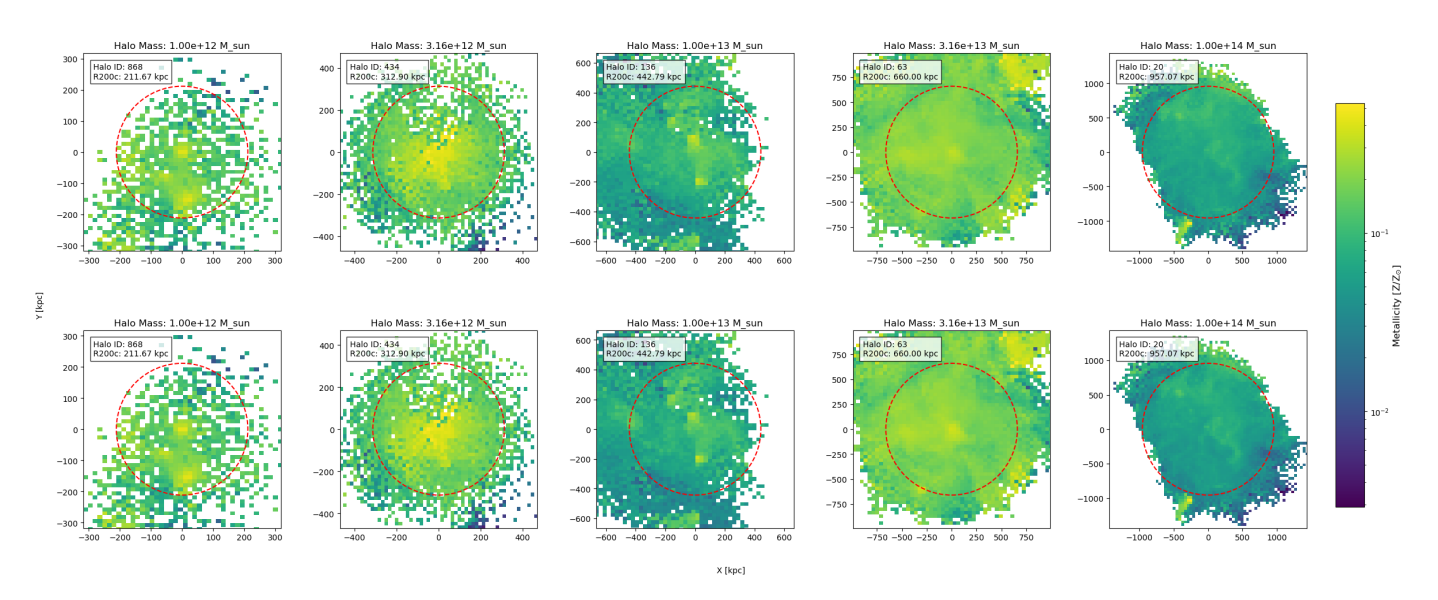


Fig. 8: 2D map of metallicity for a sample halo. The first row shows mass-weighted metallicity, and the second row shows X-ray-luminosity-weighted metallicity, calculated using equation 1. The highest metallicities are found in regions with the highest X-ray luminosity and mass.

This lack of trend in the simulation highlights a key area for further improvement in the TNG model. The feedback mechanisms, particularly AGN-driven processes, need to be refined to better match the mass-dependent gas retention seen in real clusters. Stronger feedback in lower-mass halos, combined with more efficient gas retention in the most massive systems, may help to align the simulation results with observational data.

3.3. Conclusions and Future Directions

In this research, we focused primarily on hot gas, although the stellar mass and cold gas, as shown in Figure 5, can contribute approximately 10% and 1% of the total baryonic fraction, respectively. A future direction for this work could involve creating mock observations to further explore the distribution of cold

gas and stellar mass, thereby obtaining a more complete picture of the baryonic components in galaxy clusters.

The results of our analysis suggest that the methodology used to estimate gas fractions in both simulations and observations likely leads to an overestimation of the true halo gas content. This overestimation stems from several factors, including the limitations of the modified β -model, the assumption of spherical symmetry, and the failure to account for non-thermal pressure support in observations. In simulations, the inefficiency of feedback mechanisms and the underestimation of physical processes that lead to the ejection of gas beyond the halo boundary contribute to the inflated gas fractions.

One improvement for future studies could involve replacing the Navarro et al. (1995) equation for X-ray luminosity with more accurate models, which may lead to more accurate estimates of gas fractions.

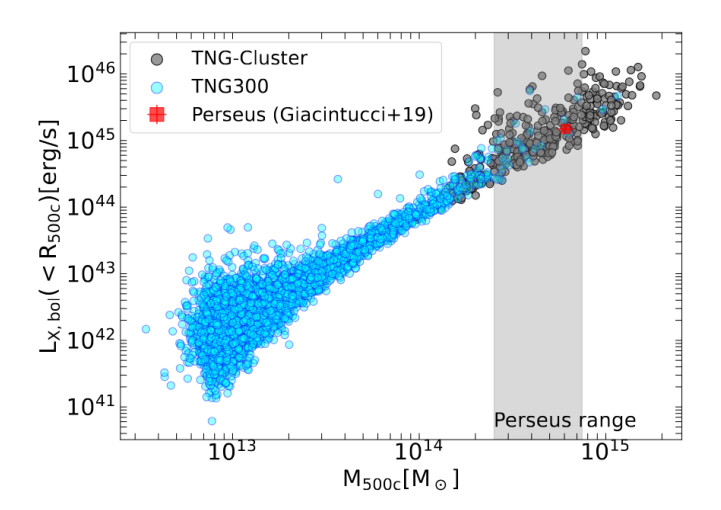


Fig. 9: Figure 1 from Truong et al. (2024): distribution of galaxy clusters derived in the $L_X M_{500c}$ plane at redshift z=0, displaying the comparison between TNG-Cluster (grey) and TNG300 (blue) simulations and the observational data of the Perseus cluster from Giacintucci et al. (2019). In the mass range of Perseus, $M_{200c}=10^{14.7-15}M_{\odot}$ (or $M_{500c}=10^{14.4}10^{14.87}M_{\odot}$), the TNG-Cluster dataset contains 135 halos.

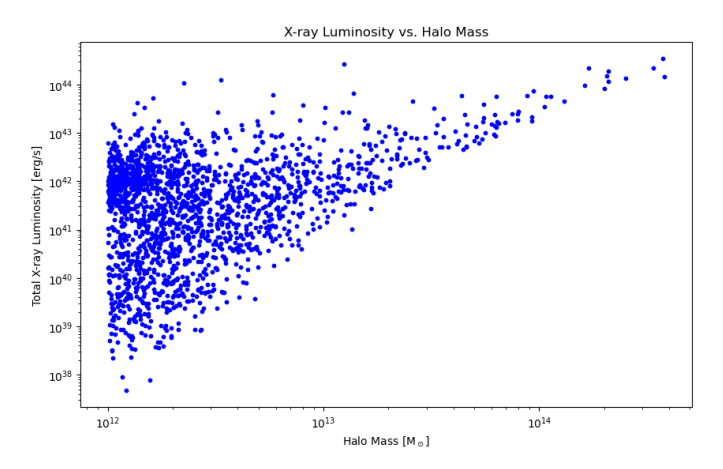


Fig. 10: X-ray luminosity, calculated using equation 1, plotted against halo mass (M_{200c}) for a range of halos. The plot shows an increase in X-ray luminosity with increasing halo mass, consistent with the general trend observed in simulations.

Finally, extending this analysis to the TNG-Cluster Simulation will provide a more comprehensive understanding of the gas fractions in the most massive halos. It will also help test whether the overestimation of gas fractions persists in higher-mass systems, allowing for a more accurate comparison between simulations and observations. This will ultimately provide deeper insights into the physical processes that regulate the baryon content of galaxy clusters.

References

References

Chiu, I., Mohr, J. J., McDonald, M., et al. 2018, MNRAS, 478, 3072
Kay, S. T. & Pratt, G. W. 2022, in Handbook of X-ray and Gamma-ray Astrophysics, ed. C. Bambi & A. Sangangelo, 100
Ma, X., Hopkins, P. F., Faucher-Giguère, C.-A., et al. 2016, MNRAS, 456, 2140

McDonald, M., Benson, B. A., Vikhlinin, A., et al. 2013, ApJ, 774, 23

Mushotzky, R. 1998, Proceedings of the National Academy of Science, 95, 72

Navarro, J. F., Frenk, C. S., & White, S. D. M. 1995, MNRAS, 275, 720
Nicastro, F., Kaastra, J., Krongold, Y., et al. 2018, Nature, 558, 406
Pratt, G. W., Croston, J. H., Arnaud, M., & Böhringer, H. 2009, A&A, 498, 361

Shull, J. M., Smith, B. D., & Danforth, C. W. 2012, The Astrophysical Journal, 759, 23

Truong, N., Pillepich, A., Nelson, D., et al. 2024, A&A, 686, A200 Zhang, Y. Y., Andernach, H., Caretta, C. A., et al. 2011, A&A, 526, A105

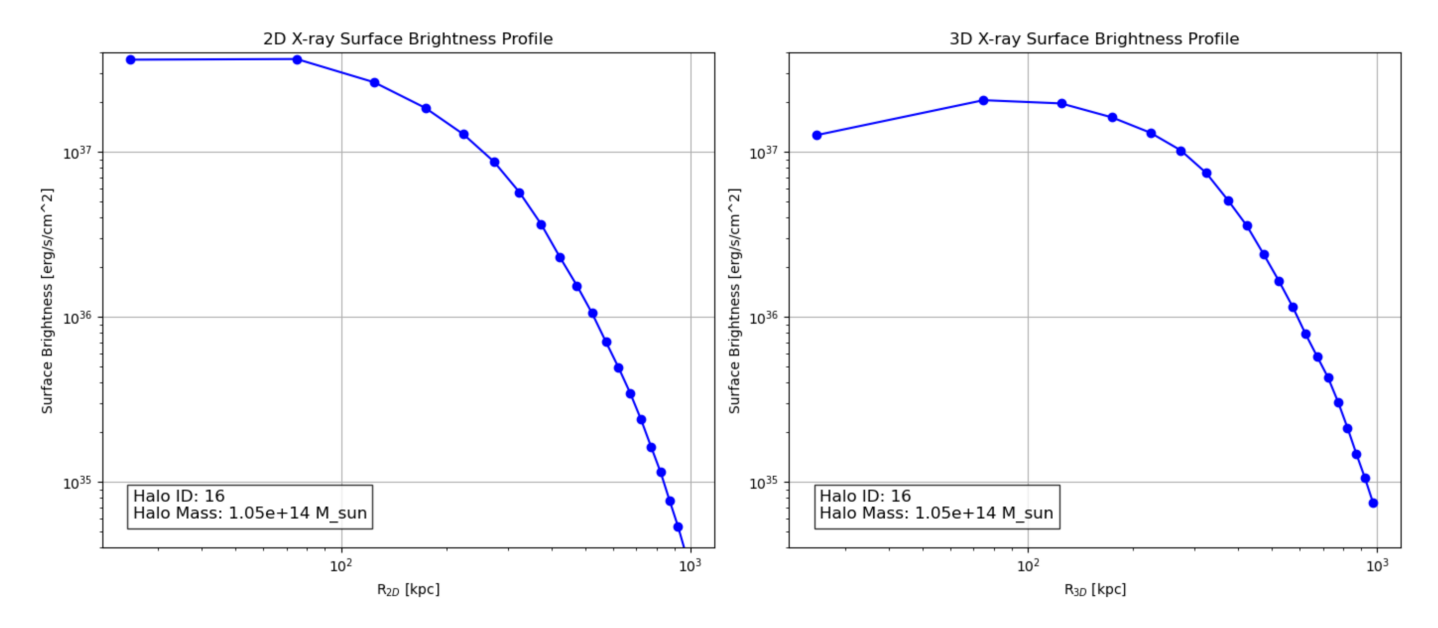


Fig. 11: Comparison of X-ray surface brightness in 2D and 3D, calculated using equation 2. The profile is plotted against radius R, with a shell thickness $\delta R = 0.05R_{200c}$. The 2D projection results in particles at larger radii appearing closer to the center when projected.

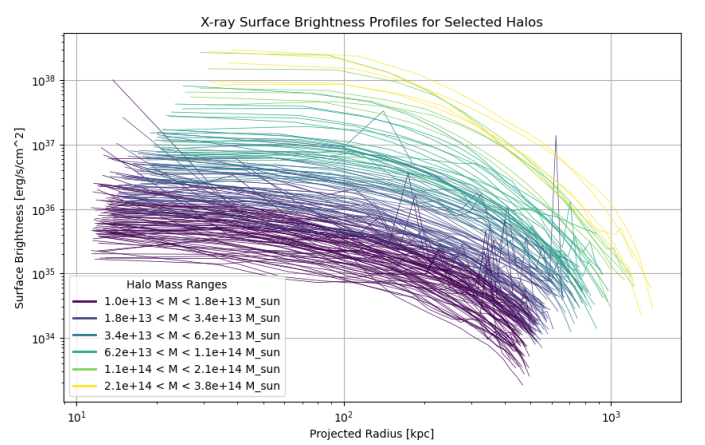


Fig. 12: X-ray surface brightness, calculated using equation 2, for all halos more massive than $10^{13} M_{\odot}$. The surface brightness is projected in 2D for each halo and plotted as a function of radius.

Fig. 13: Emissivity profile of a sample halo, fitted with the modified β -model using equation 7. The fit provides the free parameters $(n_0, \alpha, \beta, \epsilon, r_c, \text{ and } r_s)$.

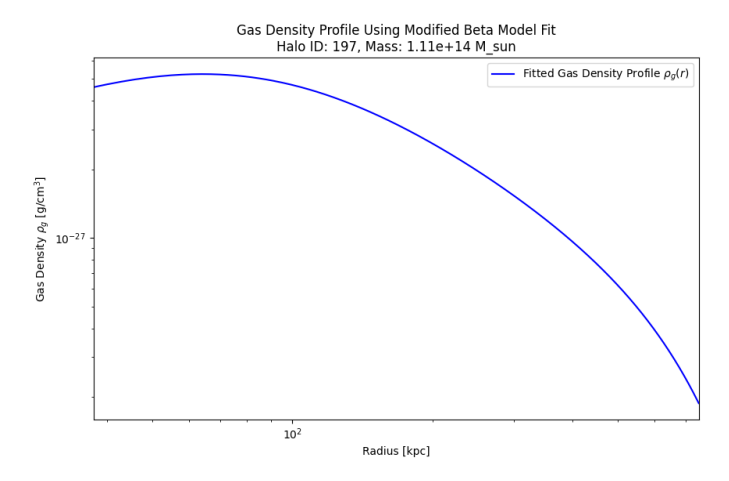


Fig. 14: Gas density profile computed using the fitted parameters from the β -model (equation 6). The thick line represents the profile of a specific cluster for which the fit was performed. Thinner lines represent the density profiles for other clusters for comparison.



Fig. 15: Top: The halo baryon fraction is computed purely using the simulation data (as shown in Figures 5, 6, and 7) for halos more massive than $10^{14}M_{\odot}$. Additionally, the mock halo baryon fraction is calculated using the methodology explained in Section 2. The solid line represents the median. Bottom: The ratio of the mock baryon fraction to the simulated baryon fraction, plotted as a function of halo mass for halos more massive than $10^{14}M_{\odot}$. The plotted line represents the median value.

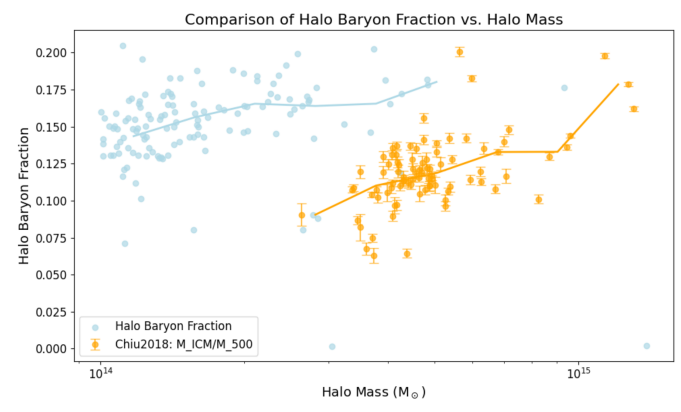


Fig. 16: The halo baryon fraction computed using the method described in Section 2 with the IllustrisTNG simulation compared with data extracted from Table 2 of Chiu et al. (2018). The observational baryon fraction is calculated by dividing $M_{\rm ICM}$ by $M_{\rm 500}$. The y-axis label represents the normalized baryon fraction.